Earth Planet. Sci. Lett. 643 (2024) 118883

Contents lists available at ScienceDirect

Earth and Planetary Science Letters

journal homepage: www.elsevier.com/locate/epsl

Induced seismicity and surface deformation associated with long-term and abrupt geothermal operations in Blue Mountain, Nevada

Roshan Koirala [a,*], Grzegorz Kwiatek [b], Manoochehr Shirzaei [c], Emily Brodsky [d], Trenton Cladouhos [e], Michael Swyer [f], Thomas Goebel [a]

[a] University of Memphis, Center for Earthquake Research and Information (CERI), Memphis, TN, USA
[b] German Research Centre for Geosciences (GFZ), Section 4.2 Geomechanics and Scientific Drilling, Potsdam, Germany
[c] Virginia Polytechnic Institute and State University, Department of Geosciences, Blacksburg, VA, USA
[d] University of California Santa Cruz, Department of Earth and Planetary Sciences, Santa Cruz, CA, USA
[e] Stoneway Geothermal, Seattle, WA, USA
[f] CyrQ Energy, Reno, NV, USA

ARTICLE INFO

Keywords:
Induced seismicity
Ground subsidence
Geothermal reservoir
Aseismic and seismic slip
Poroelastic stress
Thermal contraction

ABSTRACT

Geothermal reservoir operations can lead to seismic activity, for instance, due to increased pore pressure, but some observations are difficult to explain by pressure changes alone. Such observations include unexpected, induced events after injection well shut-in when pore pressures are thought to decrease. Here, we analyze induced seismicity up to M_L 1.5 and surface deformation in Blue Mountain, Nevada using seismic, geodetic, and hydraulic data between 2016 and 2020. This period is characterized by long-term surface subsidence of up to 1 cm/yr above the reservoir. The long-term deformation is associated with modest seismic activity but also short-lived seismicity spikes during rapid maintenance shutdowns in 2017 and 2018. The seismicity is concentrated within the geothermal reservoir at 0.5 - 2.5 km depth, similar to injection operations.

We present a numerical model of abrupt seismicity rate changes during the two shutdowns that explains the observation through short-term poroelastic effects leading to increased Coulomb stressing rates. In contrast, the long-term surface subsidence can be modeled statically by superimposing localized fault slip, and thermal contraction of the reservoir. Our findings demonstrate that poroelastic coupling drives the abrupt increase in seismic activity following well shutdown, while aseismic fault slip and thermal contraction dictate the long-term static deformation.

1. Introduction

Geothermal energy has tremendous potential and can provide base-load power in some regions of the world. As a stable, clean and sustainable energy source, electricity and heat generated from geothermal sources are predicted to rise in many nations (International Energy Agency, 2011; Lund and Toth, 2021). Nonetheless, substantial seismic hazard is associated with enhanced geothermal systems (EGS) which may have created induced events as large as Mw5.4 (Grigoli et al., 2018; Kim et al., 2018). Such events increase the risk of infrastructure damage and may result in project cancellation, like in the case of a stimulation well in Basel, Switzerland, which was abandoned after an M_L 3.4 earthquake struck in 2006 (Deichmann and Giardini, 2009). Although larger induced events during EGS projects capture scientific and public attention, most conventional geothermal reservoirs produce only microseismicity which is too small to be felt (Gaucher et al., 2015). These events can be a useful tool for understanding reservoir permeability, fault structure, and stress/strain response to injection operations.

During geothermal power generation, fluid injection and production can induce complex ground deformation, resulting in subsidence or uplift near the geothermal field. The cumulative effect of cold fluid injection and hot water or steam production can reduce reservoir pressure and/or temperature, causing subsidence (Mossop and Segall, 1997; Fialko and Simons, 2000; Juncu et al., 2017). In some cases, the region surrounding injection sites may uplift due to the increased pressure within the reservoir (Pierre et al., 2014; Zhang et al., 2023). Depending on the local geology and operational strategy, various physical

* Corresponding author.
E-mail address: rkoirala@memphis.edu (R. Koirala).

https://doi.org/10.1016/j.epsl.2024.118883
Received 12 June 2024; Accepted 6 July 2024
Available online 20 July 2024

mechanisms may contribute to the observed deformation.

The pore pressure change within the reservoir can alter the Coulomb stress, thereby triggering fault slip and seismicity (Segall and Lu, 2015; Keranen and Weingarten, 2018). Higher pore fluid pressures decrease effective normal stresses and frictional strengths of fractures and faults, promoting fault slip where shear stresses are sufficiently high (Segall and Lu, 2015; Keranen and Weingarten, 2018). The pressurized area in direct proximity of injection wells tends to be aseismic and might deform both elastically or inelastically (Pijnenburg et al., 2018; De Barros et al., 2023). In geothermal reservoirs, the thermo-elastic stresses from thermal contraction can induce subsidence and seismicity (Wei et al., 2015).

It has been established that reservoir collapse induces poroelastic stress that favors normal and thrust faulting at various distances from the reservoir (Segall, 1989). Such poroelastic stresses can also trigger earthquakes at large distances from a reservoir during fluid injection (Goebel et al., 2017). The underlying stress perturbations have a larger spatial footprint than the diffusive pore pressure zone (Segall and Lu, 2015), and can trigger seismicity on distant faults without a hydraulic connection to the reservoir (Chang and Segall, 2016; Goebel and Brodsky, 2018; Zhai et al., 2021).

Here, we study seismicity and ground deformation at Blue Mountain Faulkner 1 Geothermal Power Plant in Nevada, which has been operating as a binary power plant since 2009. Blue Mountain lies in the Basin and Range extensional province, governed by crustal thinning and localized zones of high heat flow. The region displays two major deformation phases with at least two major igneous intrusions (Wyld, 2002). The study area is located at the intersection of the regional NNE striking, west-dipping normal-sinistral fault, and ENE striking normal-dextral faults. Those major fault intersections and associated numerous splay faults created *a* more than 1 km wide, westward dipping dilatational zone of highly fractured, permeable rocks (Faulds and Melosh, 2008). This structural setting enables deep circulation of hot fluid towards the surface (Faulds et al., 2013). Lithologically, the shallow top layer consists of unconsolidated sediments with metasedimentary rocks such as quartzite, slate, phyllite, metasiltstone, metasandstone, and some limestone at larger depths (Wyld, 2002). The rocks exposed on the western slope of Blue Mountain show silicic and argillic alteration, brecciation, quartz veining, and fossil hot spring deposits, indicating prolonged hydrothermal activity in the past (Casteel et al., 2009). These features are exposed on the mountain-face just east of Blue Mountain Reservoir, located up-dip from the present-day reservoir location. Laboratory tests indicate that fractured argillite dominates the reservoir, leading to elevated porosity and permeability (Kamali-Asl et al., 2020). The wells in Blue Mountain produce fluids from fractures at a depth of around 1200 m with injection occurring at an average depth of 1700 m. Notably, the geothermal plant has not experienced felt or publicly reported earthquakes during 14 years of operation.

This study concentrates on SAR interferometry and continuous seismic records from a local network deployed in 2016. We first introduce all available data and describe spatial and temporal seismicity patterns. Next, we discuss the long-term surface deformation from Interferometric Synthetic Aperture Radar (InSAR) analysis. We explain the observed deformation using numerical models of distributed reservoir compaction and localized fault slip. Lastly, we discuss the physical mechanism of short-term seismicity spikes during maintenance shutdowns in the context of a poroelastic model with rate-dependent earthquake nucleation.

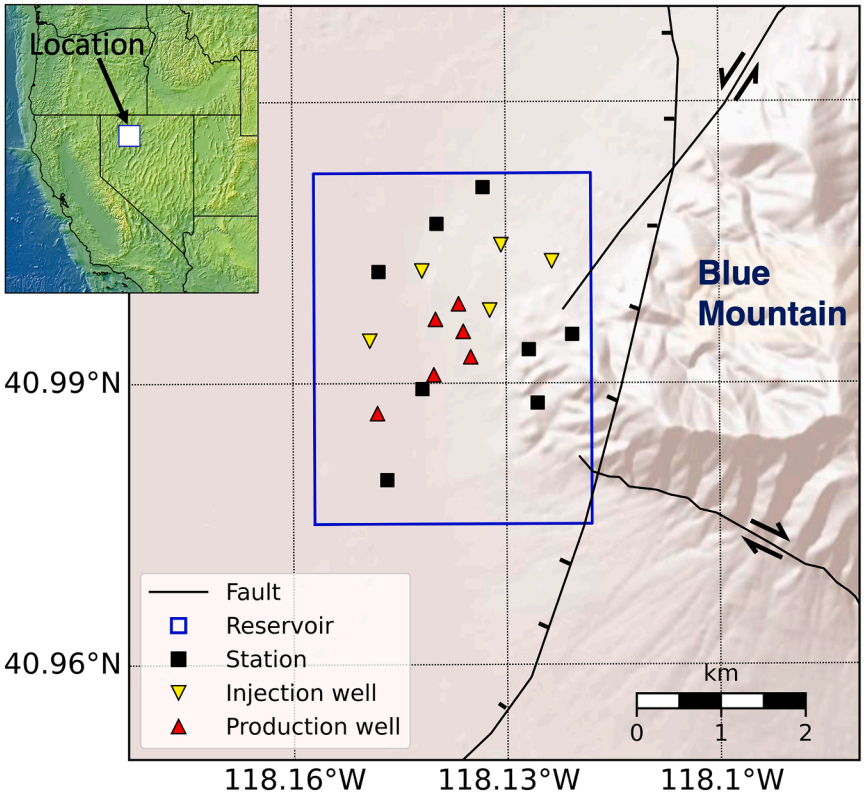

Fig. 1. Blue Mountain Geothermal Reservoir (blue rectangle) is located at the western flank of Blue Mountain within the Basin and Range province in Nevada. This map shows the locations of seismic stations (black squares), injection (yellow triangle) and production (red triangle) wells, active during the study period. The surface traces of known faults are shown by a solid black line, where the normal fault dips approximately 40° due west. Inset: Large-scale map with study area highlighted by white rectangle.

2. Data

2.1. Seismic network

We use continuous waveform data recorded by a permanent geophone array from 2016 to 2019. The array consists of eight 2-Hz, 3-component Oyo Geospace HS-1 geophones with SMART-24R digitizers recording at a sampling rate of 250 Hz (Fig. 1). Two seismic stations are deployed in boreholes at ~270 m depth, while the remaining six are buried within one meter from the surface.

2.2. InSAR data

To measure the ground deformation and generate a time series, we use Synthetic Aperture Radar (SAR) images acquired by the European Space Agency's Sentinel-1 A/B satellites from 2014/10/15 – 2021/10/22 in both ascending and descending tracks. Sentinel-1 satellites acquire SAR images in the right-looking configuration using Terrain Observation with Progressive Scans SAR (TOPSAR). Further details are shown in Table 1.

2.3. Well operation data

The operator at Blue Mountain Geothermal Rreservoir routinely monitors injection and production parameters. They granted the authors access to relative flow rates out of the geothermal powerplant and pressure changes within the scope of this project. However, absolute measurements of pressure, temperature, and flow are proprietary, and they are not essential to the conclusions of this work.

The operator changes the injection and production wells to minimize the decline in reservoir temperature while maintaining production flow rates and power generation. Therefore, not all wells are active; typically, six injection and six production wells operate simultaneously (Fig. 1).

3. Methods and results

3.1. Seismicity analysis

3.1.1. Single event locations and velocity model

Absolute earthquake locations were initially determined using a simple 1D velocity model based on active seismic measurements (Matzel et al., 2019). We then aimed to examine the location sensitivity to higher resolution 3D velocity models from the SIMULPS software package by performing simultaneous inversions for 3D velocity and event origin beginning with a 1D velocity model. However, the application of 3D velocity models resulted in nominal improvements in location because of the limited total ray-paths available to constrain high-resolution spatial inversions.

Initially, we precisely identified and selected the direct body-wave arrivals. We automatically picked P phases using a combination of a STA/LTA network detector and a single station AIC picker. We then checked and manually refined the automatically determined P-picks and manually added S-picks for each waveform using the FOCI software (version 3.9.3; Kwiatek, 2020) with additional quality control of the picks based on the signal spectrograms (Fig. 2). Next, we determined event locations using a nonlinear, probabilistic, 3-D grid-search location algorithm - NonLinLoc (NLL) (Lomax et al., 2000, 2009). We were able to detect and locate a total of 277 events with horizontal and vertical location uncertainties of 230±178 m and 315±194 m respectively. Further details about single event location are given in supplement Section I and Fig. s1.

Table 1
Sentinel 1 SAR images used in this study.

Sentinel-1	Ascending Track	Descending Track
Duration	2016/09/30 - 2021/10/22	2014/10/15 - 2021/10/14
No. of SAR Images	145	142
Heading Angle (deg)	346.36	193.60
Avg. Incidence Angle (deg)	33.74	33.93
Path No.	166	144
Frame No.	130	456

3.1.2. Earthquake relocation

We test inferences from the single event catalogs with a higher resolution relocated catalog generated using waveform cross-correlations and differential travel times of event pairs recorded at common stations using GrowClust (Trugman and Shearer, 2017). This algorithm first creates a hierarchy of event pairs based on the sum of cross-correlation values of an event pair observed at common stations. Based on the cross-correlation values, it takes in differential travel time, cross-correlation sums and starting locations of event pairs and gives new locations by minimizing the residuals between the observed and predicted differential travel times following a grid search scheme.

Here, we first perform event relocation by computing differential travel times using the picks and assigning equal weight to all the picks by allocating equal cross-correlation values to all the picks, which resulted in an unsatisfactory relocation. We then calculate the actual cross-correlation coefficient between the event pairs observed at the common stations and carry out hierarchical pairwise relocations based on the differential travel times and actual cross-correlation coefficients between event pairs.

We optimize the cross-correlation and GrowClust parameters to maximize the number of relocated events while minimizing event scattering. The corresponding parameters are: 1) a minimum single station event pair cross-correlation coefficient of 0.5, 2) a minimum average cross-correlation coefficient across the network of 0.5, 3) a maximum allowed root-mean-square differential travel time residual of 0.2 sec, and 4) maximum station distance of 20 km. This results in the relocation of 131 events out of 277 original NLLoc locations with an average horizontal and vertical precision of 99 m and 151 m, respectively.

The spatial distribution of the relocated seismicity is very similar to the original locations but with more spatial clustering close to the operation wells. Focal depths of the earthquakes range from 0.3 to 2.5 km for the relocated 131 events based on 5^{th} and 95^{th} percentiles. The reported maximum depth of the open hole segment in production wells is 1.9 km, and injection wells operate at larger depths of up to 2.5 km, which is in agreement with depth distributions of the seismic events.

Interestingly, seismicity and fault orientations from surface mapping and well-log data are approximately co-located but seismicity is not linear or planar (Fig. 3c gray color). The orientation of the westward dipping normal fault can be traced from the surface to seismogenic depth across several wells marking the fault damage zone at depth (Guo et al., 2021).

3.1.3. Local and moment magnitude estimates

We computed local magnitudes for all events following Bakun and Joyner (1984) using maximum body wave displacement amplitude (mm) and hypocentral distance (km) as the key parameters, along with additional empirical attenuation and station terms. To ensure consistency with the regional magnitude scale, we used larger magnitude regional events recorded by the Nevada Seismological Laboratory within 200 kms of Blue Mountain to compute station-specific correction terms which account for differences in site conditions (e.g., basin vs. mountain stations) (Fig. 4a,b). Very small residuals between the observed and estimated peak body wave amplitude for local events indicate that the incorporation of station correction terms improve the accuracy of magnitude calculations (Fig. 4c).

We investigate the consistency of local magnitudes through spectral analysis in the frequency domain. We check for systematically higher

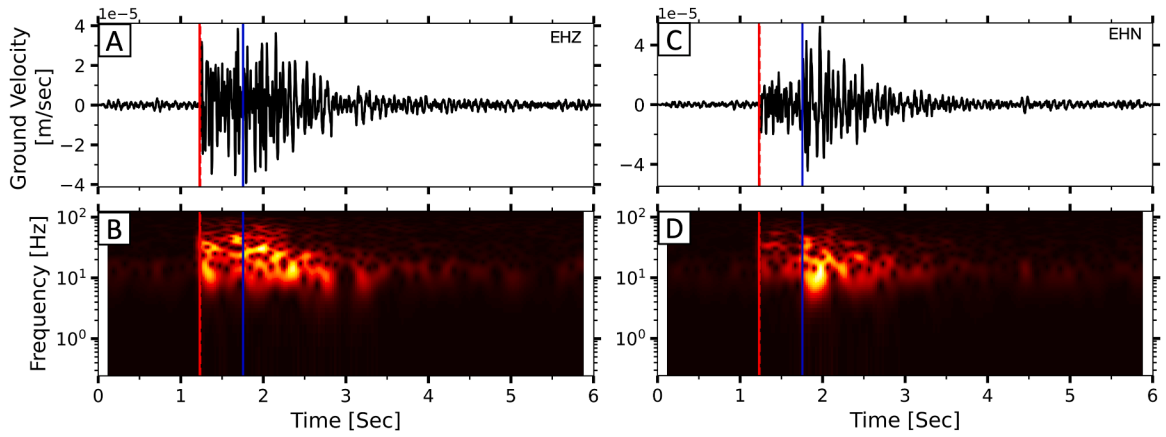

Fig. 2. Phase picking using both automated and manual methods. A, B) Vertical component seismogram and spectrogram with automatic AIC P-pick (dashed red line) and manually refined P and S-picks (solid red and blue lines, respectively) for a M_L −0.2 event with epicentral distance of 2.3 km. Note that automatic and manual P picks are almost identical for this waveform. C, D) Same as left column but for N-S component, which was used to determine the S-phase arrival.

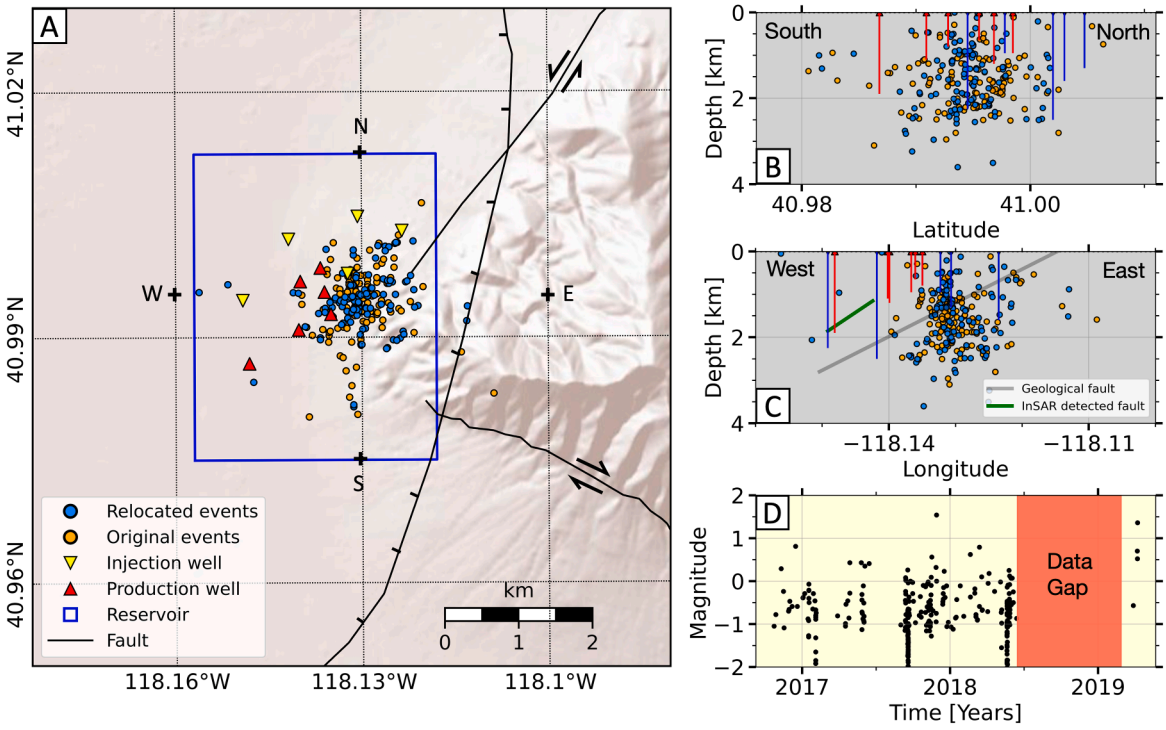

Fig. 3. Results of single-event locations (orange dots) and double-difference relocations (blue dots). A) Map view of geothermal reservoir (blue box), faults (solid black lines), injection (yellow triangle) and production (red triangle) wells and earthquakes before relocation (orange dots) and after relocation (blue dots). B) Seismicity depth section along a N-S profile through the powerplant (see N – S markers in panel A). C) Seismicity depth section along E-W profile (see E – W markers in panel A). The gray solid line represents the geologically mapped fault dipping at approximately 40°, while the green line represents the fault orientation from the InSAR inversion dipping at 59° (see Discussion and Interpretation Section 4.2). D) Distribution of earthquake magnitude through time.

corner frequencies for smaller events (Fig. s2) and calculate seismic moment and moment magnitude (M_W) based on long-period spectral amplitudes. Frequency spectra are calculated using a multi-taper/multi-window approach (Prieto, 2022).

Local and moment magnitudes are linearly related across the range of small, induced events with M_L −2.2 to 1.5 and larger regional events with M_L 1.6 to 3.8 (Fig. s3). We observe a systematic underestimation of local magnitudes for the smallest events (M_L<−1.0), likely due to the biased peak amplitude measurements related to the corner frequencies being close to the upper limit of the measured frequency band.

We use the Reno-Lab catalog to determine the regional magnitude of completeness (M_c) based on measuring the goodness-of-fit between observed and modeled Gutenberg-Richter distribution (Wiemer, 2000; Clauset et al., 2009). The M_c is 1.7 (Fig. s4) which is consistent with our local maximum magnitude event of 1.5, which, as expected, was not recorded by the regional array.

3.1.4. *Seismicity rate and migration analysis*

The geothermal power plant experiences annual maintenance shutdowns for approximately 36 to 48 h (Fig. 5a). The September 2017 and May 2018 shutdowns are followed by notable seismicity rate spikes for approximately 100 h, after which rates return to the long-term average (Fig. 5b-c). Approximately 35% of all events occur during the most seismically active shutdown period, i.e., in the first 48 h following the

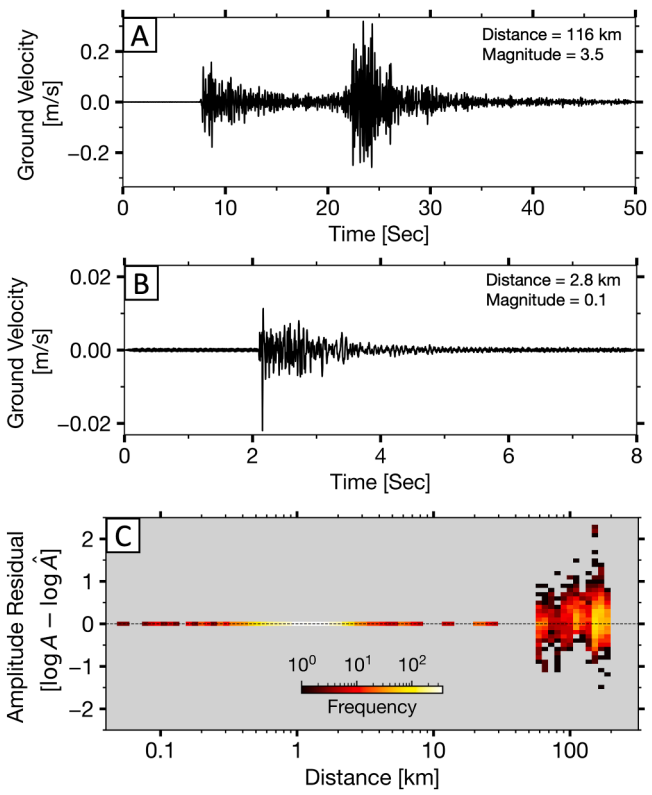

Fig. 4. Seismograms and body-wave magnitudes of a regional M_L3.5 and a local M_L 0.1 event that were both recorded by the same station in Blue Mountain. A) Regional event with M_L 3.5 at 116 km distance. B) Induced event with M_L 0.1 at a distance of only 2.8 km. C) Peak body wave amplitude residuals between observed and estimated amplitudes for each event-station pair after distance and station corrections. Local events within Blue Mountain are shown up to a distance of 10 km and regional events at distances between 60 and 200 km.

shutdown. Furthermore, the seismicity rate increase that extends beyond that of the most active period accounts for 42% of all recorded events. The remaining 58% of events occur at low rates throughout regular geothermal operation. However, another shutdown in March 2019 did not cause seismicity spikes comparable to 2017 and 2018. Conversion of injection well 44–14 into a production well two months prior to the March 2019 shutdown might have resulted in a modification of the stress field. The signal variances before, during, and after shutdown are similar (Fig. s5), indicating that the likely operational noise reduction during the shutdown has no discernible effect on earthquake detection and rate calculations.

We searched for a systematic spatiotemporal migration of seismicity; however, no significant statistical support was obtained for a diffusive square root migration from injection wells or from the first event of the sequence (Fig. s6).

In summary, the seismicity analysis revealed spatial event clustering within the geothermal reservoir with low background seismic activity and rapid rate increase after maintenance shutdown. Next, we explore how InSAR measurements complement our seismicity analysis by providing a comprehensive understanding of subsurface processes and ground deformation patterns.

3.2. InSAR

We employ a multitemporal SAR interferometric approach to map the surface deformation time series using the algorithm - Wavelet-Based InSAR (WabInSAR) (Shirzaei, 2013; Shirzaei et al., 2017; Lee and Shirzaei, 2023). For this purpose, we obtain C-band Sentinel 1A/B SAR images as tabulated in Table 1. We apply multi-looking factors of 14 in range and 2 in azimuth directions, resulting in a pixel size of ~32 m x ~28 m. Then, we perform image co-registration using satellite precise ephemeris data and a Shuttle Radar Topography Mission (SRTM) Digital Elevation Model (DEM) and apply the Enhanced Spectral Diversity algorithm (Shirzaei et al., 2017). Next, considering thresholds of 500 m for perpendicular and 700 days for temporal baselines, we create 705 and 778 interferograms for ascending and descending tracks, respectively. We remove the flat earth and topographic effects using a 3-arc-second (90 m) SRTM DEM and satellite precise ephemeris data. After identifying less noisy pixels (elite pixels), we unwrap the interferogram phases using a 2D-minimum-cost-flow algorithm (Costantini, 1998) suitable for sparsely distributed pixels (Costantini and Rosen, 1999). After correcting unwrapped interferograms for the atmospheric delay (Shirzaei and Bürgmann, 2012; Lee and Shirzaei, 2023) and orbital errors (Shirzaei and Walter, 2011), we apply the reweighted least square method to obtain the Line of Sight (LOS) displacement time series and the velocity of each pixel (Shirzaei, 2013). Eventually, both ascending and

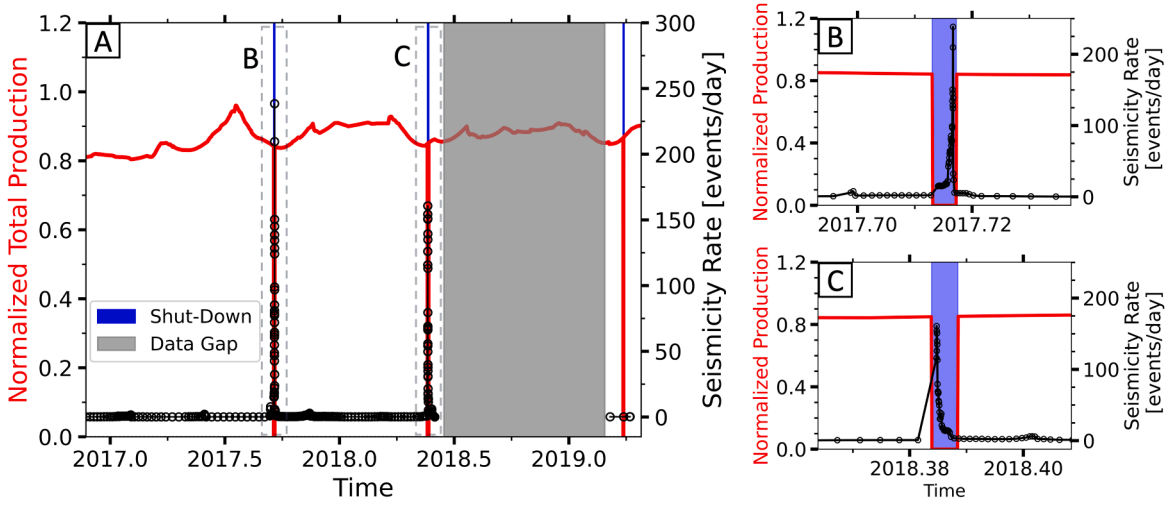

Fig. 5. Production flowrate and seismicity rate between 2017 and 2019. A) Normalized total production flowrate over the geothermal field (red curve) and seismicity rate (black curve) for the analyzed period which includes two maintenance shutdowns in September 2017 and May 2018 showing sudden seismicity rate increase during shutdown periods. No seismic data was recovered between June 2018 and February 2019 (grey, shaded area). The close-up view of seismicity rate increase in 2017 and 2018 shutdowns indicated by box B and C are shown in panel B) and C) respectively.

descending LOS displacements (Fig. s7(a), and Fig. s8(a)) with associated uncertainties (Fig. s7(b), and Fig. s8(b) see supplement) are mapped.

To combine the ascending and descending LOS displacements time series and determine the vertical and east-west time series for each overlapping pixel, we first identify the temporal overlap between ascending and descending datasets. We assume that the North-South ground motion is negligible, as the satellite with a near-polar orbit cannot detect ground deformation in that direction. Then, considering the satellite unit vectors (Hanssen, 2001), we resolve the vertical and east-west components of the deformation field from ascending and descending LOS observations (Miller and Shirzaei, 2015).

The resolved vertical surface deformation reveals a subsidence rate of up to 10 mm/yr toward the center of the geothermal reservoir (Fig. 6). East-west profiles across the reservoir are not symmetric, indicating secondary topographic or geological controls on subsidence rates. In addition, we observe potential erosional hillslopes denoted by blue dots to the east of the geothermal region, but no ground truthing is currently available. Furthermore, we observe two subtle uplift signals of 2–3 mm/yr ± 0.04 mm/yr amidst potential artifacts of atmospheric effects. The first uplift, located southeast of the study region and south of Blue Mountain, may be due to deposited erosional material transported south from the topographically higher Blue Mountain. The second uplifting region is located immediately west of the reservoir and may be caused by injected fluids migrating outside of the reservoir. However, we view these uplift signals as possibilities that require confirmation through ground truthing. The largest vertical surface deformation of ~10 mm/yr, 4.8 cm total, coincides with the operation footprint of the geothermal powerplant and is slightly elongated along the production zone (Fig. 6c, d).

In addition to the described spatial variability of surface deformation, we also analyzed temporal variations in vertical ground displacements. The corresponding time series of deformation at the center of the reservoir is dominated by subsidence at an average rate of 10 mm/yr (Fig. 6c,d).

We observe some deviations from this average rate with noticeable acceleration in the second half of 2018 and 2020 with deformation velocities of 16.8 mm/yr and 16.4 mm/yr respectively (Fig. 6d). We check for seasonal and precipitation effects but find no direct correlations with the periods of accelerated deformation, suggesting that operational changes are key drivers of subsidence above the reservoir.

4. Discussion

The results above show that the reservoir responds to long-term geothermal energy production with continuous subsidence and low seismic activity while exhibiting an abrupt increase in seismicity following well shutdowns. This section discusses plausible physical mechanisms for the observed subsidence and seismicity.

4.1. Mechanisms of long-term surface subsidence

Studies have demonstrated that geothermal reservoirs may exhibit ground deformation and microseismicity (Mossop and Segall, 1997; Majer et al., 2007), similar to hydrocarbon reservoirs (Segall et al., 1994). Geothermal reservoirs have the potential to undergo deformation

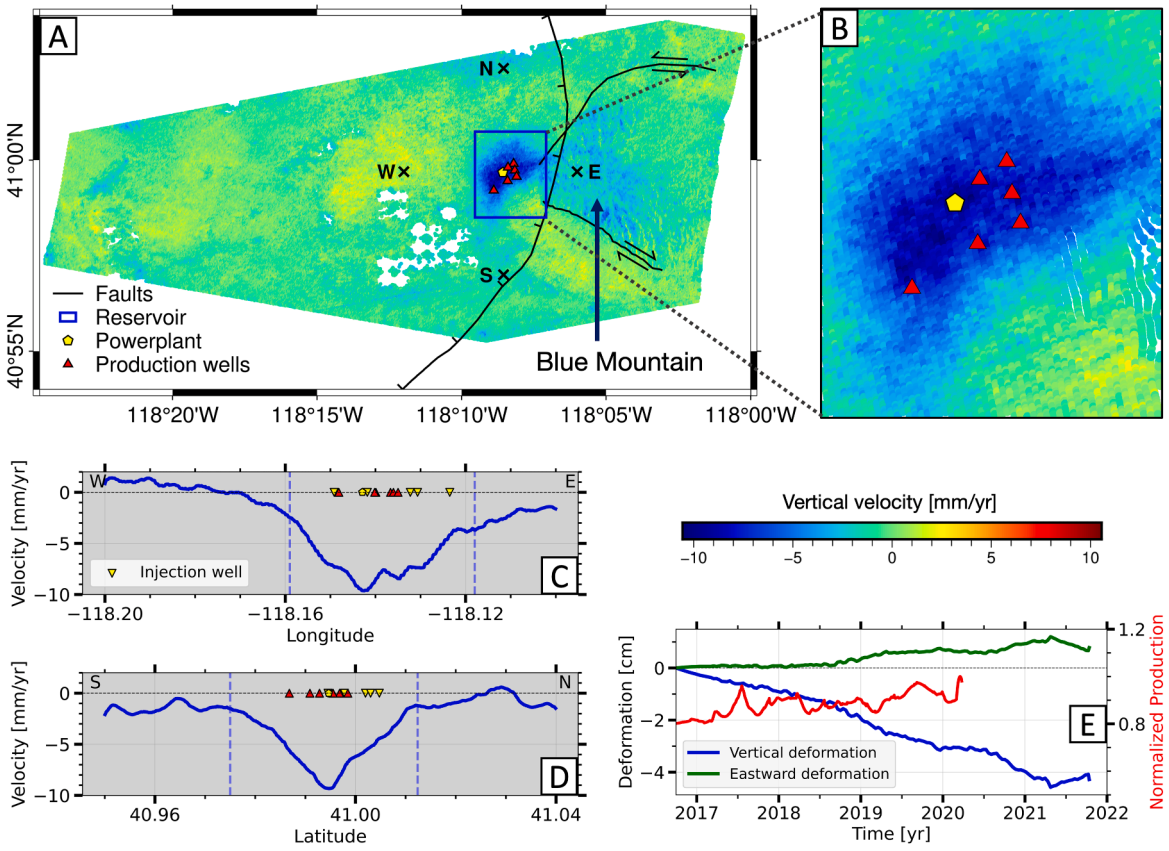

Fig. 6. Ground deformation mapping performed using Sentinel-1 SAR images. A) Cumulative vertical displacement resolved from the combination of LOS displacement in ascending and descending tracks. The blue rectangle represents the geothermal area, black line with ticks represents the normal fault, and black lines with arrows pointing in opposite directions represent strike-slip faults. B) A magnified view of the ground deformation around the geothermal area. C) Vertical deformation rate along west – east profile (see W – E markers in panel A). The dashed blue line represents the geothermal boundary in panel A. D) Vertical deformation rate along north – south profile (see N - S in panel A), where both profiles indicate maximum velocity occurring at the center of geothermal operations. E) Total vertical (blue) and eastward (green) deformation time series around the maximum deformation area and normalized cumulative fluid production (red).

as a result of many factors, such as thermoelastic and poroelastic stresses (Martínez-Garzón et al., 2014), as well as seismic and aseismic fault slip along preexisting faults (Mossop and Segall, 1997; Pijnenburg et al., 2018).

Here, we seek to explain the observed InSAR surface deformation using the simplest yet plausible models, i.e., localized fault slip, volumetric contraction and pore space collapse in a homogenous half-space. The simple solutions are not meant to capture the full complexity of Blue Mountain, but to provide first-order insight into dominant deformation mechanisms and their relative importance.

We test whether the surface deformation is likely a result of distributed deformation or localized slip on preexisting faults. We compare theoretical and observed deformation using three different models: 1) a decoupled Mogi-model for temperature decline induced rock volume contraction (Mogi, 1958; Segall, 2010), 2) a fluid mass point source solution for poroelastic deformation (Rudnicki, 1986) to investigate land subsidence due to distributed volumetric changes, and 3) an Okada model of slip on a rectangular fault (Okada, 1985). Note that fault slip in the Okada model could be seismic or aseismic; however, the lack of notable seismicity suggests that slip would have to be aseismic (see moment balance calculation below). We begin by analyzing Mogi, Okada, and poroelastic point sources separately and report the respective misfit to identify primary deformation mechanisms. We then invert for the best combined solution that matches the observed subsidence pattern (Fig. 7a).

The respective surface deformation due to reservoir contraction or expansion from temperature changes was estimated using a Mogi solution (e.g., Segall, 2010):

$$u_z = \frac{(1-\nu)\Delta V}{\pi} \frac{d}{\left(\rho^2 + d^2\right)^{3/2}}, \tag{1}$$

where, $\Delta V = e_{kk} V$ is the change in reservoir volume (V), $e_{kk} = \alpha_v \Delta T$ is volumetric strain, α_v is the coefficient of volumetric expansion, ΔT is temperature changes, d is depth to the reservoir centroid from the surface, and ρ is the radial coordinate along the free surface.

The Okada model resolves the best-fitting rectangular fault orientation and depth in an elastic half-space employing a least-squares approach. This model establishes a relationship between ground deformation and various fault parameters. These parameters include fault dimensions, slip direction and magnitude, depth, three-dimensional orientation, and the elastic properties of the host rock.

While Okada and Mogi provide simple kinematic solutions, the poroelastic model integrates over the observed injection and production time series and is also used to model seismicity rate changes in the following section. To evaluate the contribution of poroelastic coupling

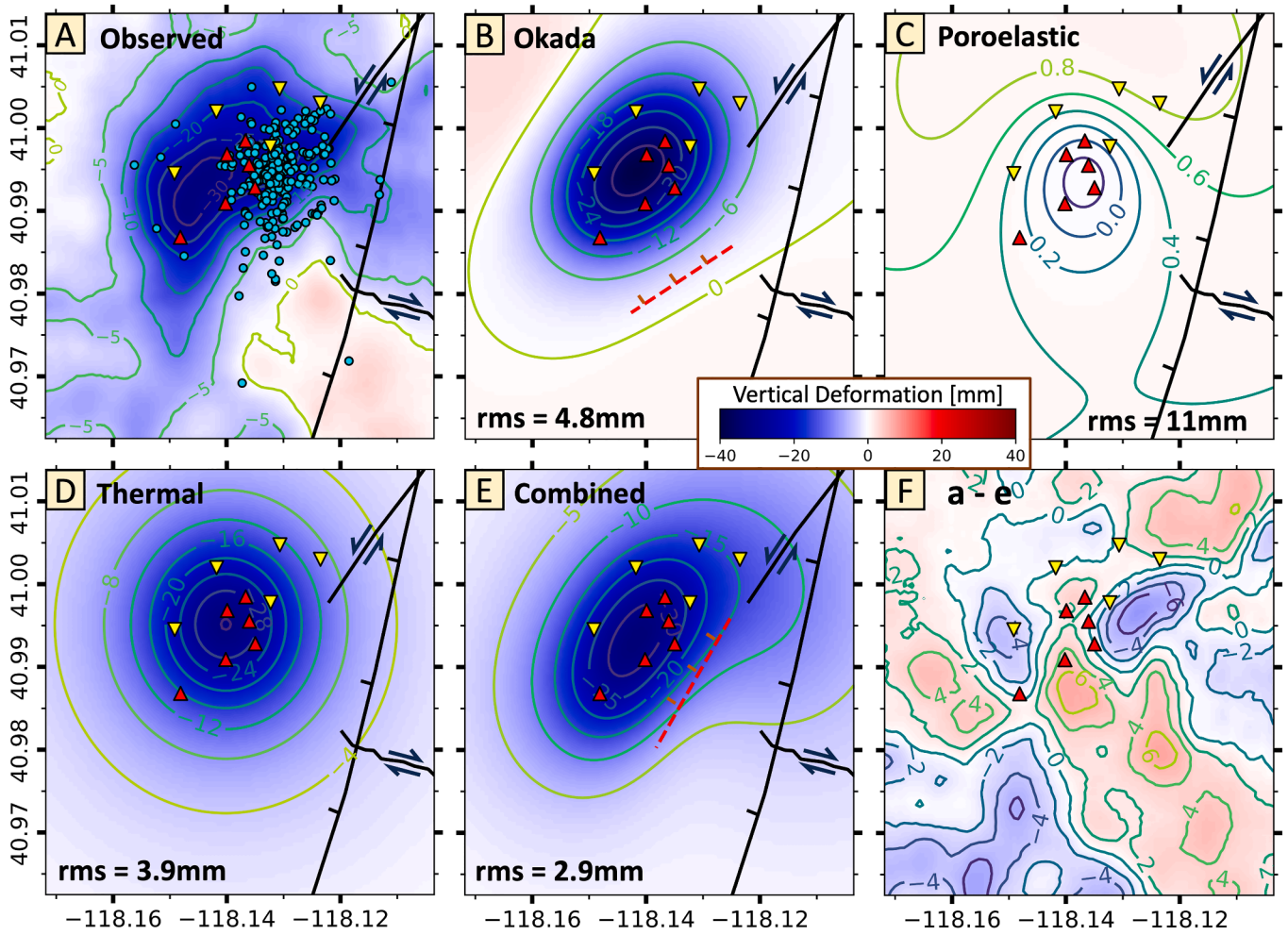

Fig. 7. Observed surface deformation from InSAR mapping, and inversion results using three different plausible deformation sources: i) localized slip on a rectangular fault, and ii) temperature and iii) pressure decline within a spherical cavity. Panels A-E show surface deformation from InSAR observations with seismicity (white dots) on top (A), Okada (B), Point mass source (C), Thermal Mogi source (D), and a combined Okada+Mogi+Point Source model (E). Panel F shows misfit between a and e. The colormap shows vertical ground deformation (blue – subsidence, red - uplift), contours – ground deformation contours, toothed lines - normal faults (black lines existing faults and red lines faults from inversion), lines with parallel arrows pointing opposite direction - strike slip faults, red triangles – production wells, yellow triangles – injection wells.

to the observed subsidence, we computed the deformation driven by the pressure changes associated with point source fluid injection and production within a homogeneous medium based on (Rudnicki, 1986; Eq. 2).

$$U_i(x,t) = \frac{Qx_i}{Dr}\left[\frac{\lambda_u - \lambda}{8\pi\alpha(\lambda_u + 2G)}\right]u(\xi) \tag{2}$$

$$u(\xi) = \mathrm{erfc}\left(\frac{1}{2}\xi\right) + 2\xi^{-2}g(\xi)$$

$$g(\xi) = \mathrm{erf}\left(\frac{1}{2}\xi\right) - \frac{\xi}{\sqrt{\pi}}e^{-\frac{1}{4}\xi^2}$$

$$D = \frac{k2G(1-\nu)(\nu_u - \nu)}{\eta\alpha^2(1-2\nu)^2(1-\nu_u)}$$

Where, Q is fluid injection rate, k is permeability, α is Biot coefficient, r is distance, x_i is direction component, G is shear modulus, t is time, D is hydraulic diffusivity, λ_u, λ are drained and undrained Lame parameter, ν, ν_u are drained and undrained Poisson's ratio, $\xi = \frac{r}{\sqrt{Dt}}$ is similarity variable for the diffusion process.

The simple homogeneous half-space models suggest that both distributed volumetric sources and localized slip contribute to the observed surface deformation (Fig. 7). The respective misfits are rms= 3.9 mm for thermal contraction, rms= 4.8 mm for localized fault slip, and rms= 11 mm for poroelastic reservoir collapse (Fig. 7). Note that although the misfit is lowest for the thermal Mogi model, the Okada fault slip provides a better geometric match of the observed surface deformation pattern. The poroelastic solution does not capture the observed deformation field which is apparent when comparing model solution to a zero-displacement scenario, which has a misfit rms of 10.7 mm.

To further test the relative contributions from Mogi, Okada and poroelastic models, we perform a combined optimization which, expectedly, yields superior results (Fig. 7e and F, misfit rms= 2.9 mm) compared to the individual models. The combined inversion produces a west-dipping normal fault which provides a better match to the known fault orientation than the individual solutions (compare red and black normal faults in Fig. 7b and e and fault parameters in Table 2).

The best-fit model (Fig. 7e) suggests that the subsidence volume from rectangular fault slip accounts for 63% of the observed InSAR-measured subsidence volume, thermal contraction for 36%, and poroelastic coupling for less than 1% of the total observed subsidence. Relative contributions are based on deformation budgets for each model, derived from joint optimization as a proxy for their relative contribution to the overall subsidence. We conclude that fault slip and thermal contraction are the primary mechanisms driving subsidence, with poroelastic coupling resulting in minimal surface subsidence.

To further characterize long term deformation mechanisms, we compare total observed seismic moment and theoretically expected deformation moment from InSAR. The measured InSAR subsidence can be converted to an equivalent seismic moment using $Mo = G\Delta V$ (also known as deformation moment, where ΔV = subsidence volume; G = shear modulus , Mcgarr, 1976), assuming that the ground deformation is entirely seismic. We find that the cumulative seismic moment accounts for less than one percent of the total deformation moment so that long term deformation is predominantly aseismic.

Table 2
Fault parameters.

Strike	Dip	Rake	Length (km)	Width (km)	Centroid Depth (km)	Slip (m)
I. Okada only optimization						
240	*37.8*	*−73*	*1.9*	*1.4*	*1.5*	*0.24*
II. Joint Mogi, Okada, and Poroelastic optimization						
213	*59*	*−109*	*2.0*	*0.5*	*1.5*	*0.29*

Previous studies have demonstrated that a significant proportion of moment release in geothermal reservoirs is aseismic. Examples include the Brawley geothermal reservoir with 34% aseismic deformation (Materna et al., 2022), and Cooper Basin with 40–60% aseismic moment release (Wang and Dunham, 2022). Since the cumulative seismic moment of Blue Mountain earthquakes is 4.5×10^{-5}% of the total InSAR deformation moment calculated using $Mo = G\Delta V$, the moment from fault slip is predominantly aseismic.

We identified three plausible long term deformation mechanisms: 1) fault slip, 2) temperature decline induced rock contraction, and 3) poroelastic coupling. Although poroelastic effects were deemed minor for long term deformation, they may still affect short term seismicity transients. In the following, we investigate the mechanism behind the rapid seismicity rate increase following well shutdowns.

4.2. Mechanisms of short-term seismicity spikes during maintenance shutdown

In addition to long-term subsidence, we observed short-term seismicity rate spikes associated with abrupt maintenance shutdowns. The abruptness and short duration of the seismicity rate increase suggest that a combination of diffusive processes and rapid stress changes are likely to have caused the earthquakes. Temperature changes during operational pauses have essentially no effect on seismicity at distances between 0.2 and 2 km within ~48 h for reasonable thermal diffusivities of rock.

We investigate whether the coupling between pore pressure changes and associated poroelastic stresses can plausibly explain the observation. To evaluate whether pore pressure and poroelastic effects provide a plausible explanation for the observed induced microseismicity, we model seismicity rate changes as a function of well flowrate changes in a fully coupled homogenous reservoir subject to rapid injection shutdown and time-dependent earthquake nucleation (Segall and Lu, 2015). Segall and Lu (2015) present a simplified version of the seismicity rate model proposed by Dieterich (1994), which asserts that under favorable background stress conditions, Coulomb stress changes govern seismic activity on fault systems with rate-and-state friction.

To assess the role of Coulomb stressing rates, we first calculate pore pressure, p, and poroelastic stress, σ_{ij}, for a fluid injection point source, utilizing the injection history in conjunction with hydrological and mechanical parameters of the 3D homogeneous reservoir (Table 3) (Rudnicki, 1986):

$$p = \frac{Q\,\eta}{4\pi r\,k}\,erfc\left(\frac{1}{2}\xi\right) \tag{3}$$

$$\sigma_{ij}(x,t) = -\frac{Q(\lambda_u - \lambda)G}{4\pi Dr\alpha(\lambda_u + 2G)}\left\{\delta_{ij}\left[\mathrm{erfc}\left(\frac{1}{2}\xi\right) - 2\xi^{-2}g(\xi)\right] + \frac{x_i x_j}{r^2}\left[\mathrm{erfc}\left(\frac{1}{2}\xi\right) + 6\xi^{-2}g(\xi)\right]\right\}, \tag{4}$$

Table 3
Model parameters used in this study.

Parameter	Variable	Value and Units
Poroelastic properties		
Shear modulus	G	20 GPa
Drained Poisson's ratio	ν	0.25
Undrained Poisson's ratio	ν_u	0.3004
Biot Coefficient	α	0.7
Transport properties		
Fluid Viscosity (@ 100 °C)	η	2.814 * 1e-4 PaS
Fluid Density	ρ	10^3 kg/m^3
Permeability	k	$4 \times 10^{-14} - 6 \times 10^{-15}$ m^2
Friction properties and stress rate		
Coefficient of friction	f	0.6
Effective normal stress	$\bar{\sigma}$	Function of depth
Background stressing rate	$\dot{\tau}_0$	0.001 MPa/yr

where, η is fluid viscosity, i and j indicate directional indices in 3D, G is shear modulus, and δ is the Dirac delta function. In a poroelastic framework, Eq. (4) incorporates the coupling between pore pressure and rock deformation to determine the stress tensor. Equation (1) on the other hand leverages this coupling to relate well flowrate to displacement and strain.

From the poroelastic stress tensor, normal and shear stresses operating on a fault plane are subsequently determined. We then compute Coulomb stress (τ) through $\tau = \tau_s + f(\sigma + p)$, where f represents the coefficient of friction, p denotes the pore pressure, and τ_s and σ represent the shear and normal stresses respectively, acting on the fault plane.

In light of the assumption that slip is primarily concentrated along normal faults optimally oriented within the principal stress field, the seismicity rate is calculated using (Segall and Lu, 2015):

$$\frac{dR}{dt} = \frac{R}{\tau_a}\left(\frac{\dot{\tau}}{\dot{\tau}_0} - R\right), \tag{5}$$

where, R is the seismicity rate relative to the steady-state background seismicity rate, $\dot{\tau}$ is Coulomb stressing rate, $\dot{\tau}_0$ is background stressing rate, $\tau_a \equiv \frac{a\bar{\sigma}}{\dot{\tau}_0}$ is the characteristic relaxation time, a is the fault constitutive friction parameter quantifying the direct effect on slip rate, and $\bar{\sigma}$ is background effective normal stress.

Here, we model the increase in seismicity rate associated with two shutdown occurrences, on September 18, 2017 and May 21, 2018 with respect to flow rate modifications in all operational wells. The seismicity rate is modeled on a network of small faults that are optimally oriented within the principal stress field. These faults experience both pressure and poroelastic stress changes (Eq. 3–4) due to fluid injection and production in wells for the reservoir properties enlisted in Table 3. The pore pressures and stresses used for seismicity rate calculations are determined from a linear superposition of all injection and production wells.

During pressure, stress and seismicity rate modeling, most parameters remain unchanged over space and time except for reservoir permeability (k), effective normal stress ($\bar{\sigma}$) and characteristic relaxation time (τ_a), which are varied within a plausible range, i.e., based on prior measurements of tidally induced water level changes in idle wells (Guo et al., 2021). Relaxation time τ_a depends on three parameters (a, $\bar{\sigma}$ and $\dot{\tau}_0$) leading to inherent tradeoffs between them.

In the following, we compare temporal and spatial seismicity patterns in the rate-and-state models with observations in Blue Mountain. The 2018 shutdown is characterized by a single-step cessation in flowrate, followed by coulomb stress increase (Fig. 8c), and subsequent increase in seismic activity (Fig. 8d). The seismicity rate that reaches up to a peak amplitude of 129 events/day during shutdown is accompanied by an exponential rate decay (Fig. 8d). The initial seismicity rates for two days after the 2018 shutdown conform well to the modeled rates (see solid curve in Fig. 8d). This is followed by higher observed seismicity rates than the model, potentially due to spatially distinct relaxation times on faults at larger distance (see dashed curve in Fig. 8d). The observed seismicity rate is most accurately represented by the model parameters $k = 4 \times 10^{-14}$ m^2 and $\tau_a = 300$ days during the main surge and the same k with $\tau_a = 1100$ days during the later decay phases with other static parameters as enlisted in Table 3.

Seismicity rates in 2017 are more complex than in 2018. The 2017 shutdown experienced a two-step reduction in the well flowrate, including an approximate 20% decline six days before the shutdown and complete injection/production cessation on September 18. Each flowrate decline is promptly succeeded by increase in coulomb stress (Fig. 8a), and subsequent upsurge in seismic activity with emergent onset of 6 to 20 events/day, followed by pronounced peaks of 60 to 500 events/day several hours later (Fig. 8b, black circle). The difference between 2017 and 2018 may indicate a larger degree of heterogeneity during the earlier injection period and evolution toward a more homogeneous system. A potential explanation is a larger degree of spatial heterogeneity in reservoir permeability structure, which exhibits long-term evolution e.g., due to dissolution processes (Swyer, 2021).

During maintenance shut-downs, both pore pressures and absolute normal stresses begin to decline, albeit at distinct space-time scales. Pore pressures remain elevated for longer at larger distances due to the inherent time lag of pressure diffusion (Hsieh and Bredehoeft, 1981; Goebel et al., 2017), whereas normal clamping (negative) stress is reduced resulting in increased Coulomb stress on optimally oriented faults (Fig. 8a, c).

To unravel direct pressure and poroelastic effects, we calculate respective Coulomb stress distributions across the geothermal reservoir (Fig. 9). This calculation incorporates well flowrates and considers the Euclidean distance from each well trajectory to every grid node in a 2D depth-slice. Pressure recovery around production wells leads to localized positive Coulomb stress change which is most visible for the southernmost producer (Fig. 9a, c). Incorporating poroelastic coupling in the Coulomb stress calculations significantly expands the zone of stress increase to encompass the seismically active regions (Fig. 9b, d). The poroelastic stresses exhibit a strong azimuthal dependence with most significant stress increase in the σ_3 direction, which conincides with the direction of induced events. Both injection and seismicity are

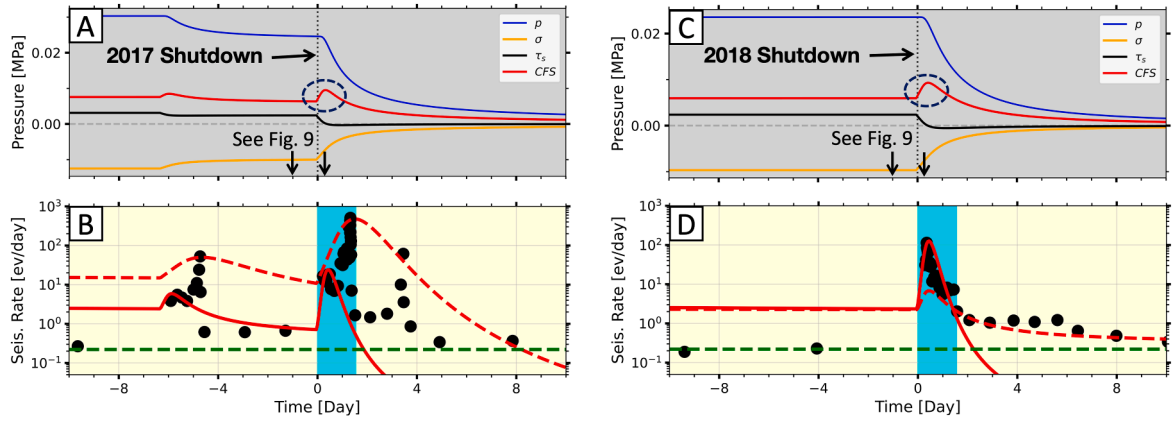

Fig. 8. Expected and observed temporal seismicity rate changes associated with geothermal operation shutdowns at the seismicity centroid. A) Temporal evolution of pore pressure, shear, normal (negative normal stress indicates fault clamping) and Coulomb stresses associated with geothermal shutdown in 2017. Two vertical gray arrows represent the start and end times used to calculate the Coulomb Stress changes presented in Fig. 9. B) Seismicity rate change after 2017 shutdown. The measured seismicity rate is represented by black dots. The solid red and dashed red curves represent expected seismicity rate for 'high permeability with smaller τ_a', and 'low permeability with larger τ_a' respectively. The light-blue color bar represents shutdown period Panels C, and D represent similar observation to A, and B respectively, for 2018 shutdown.

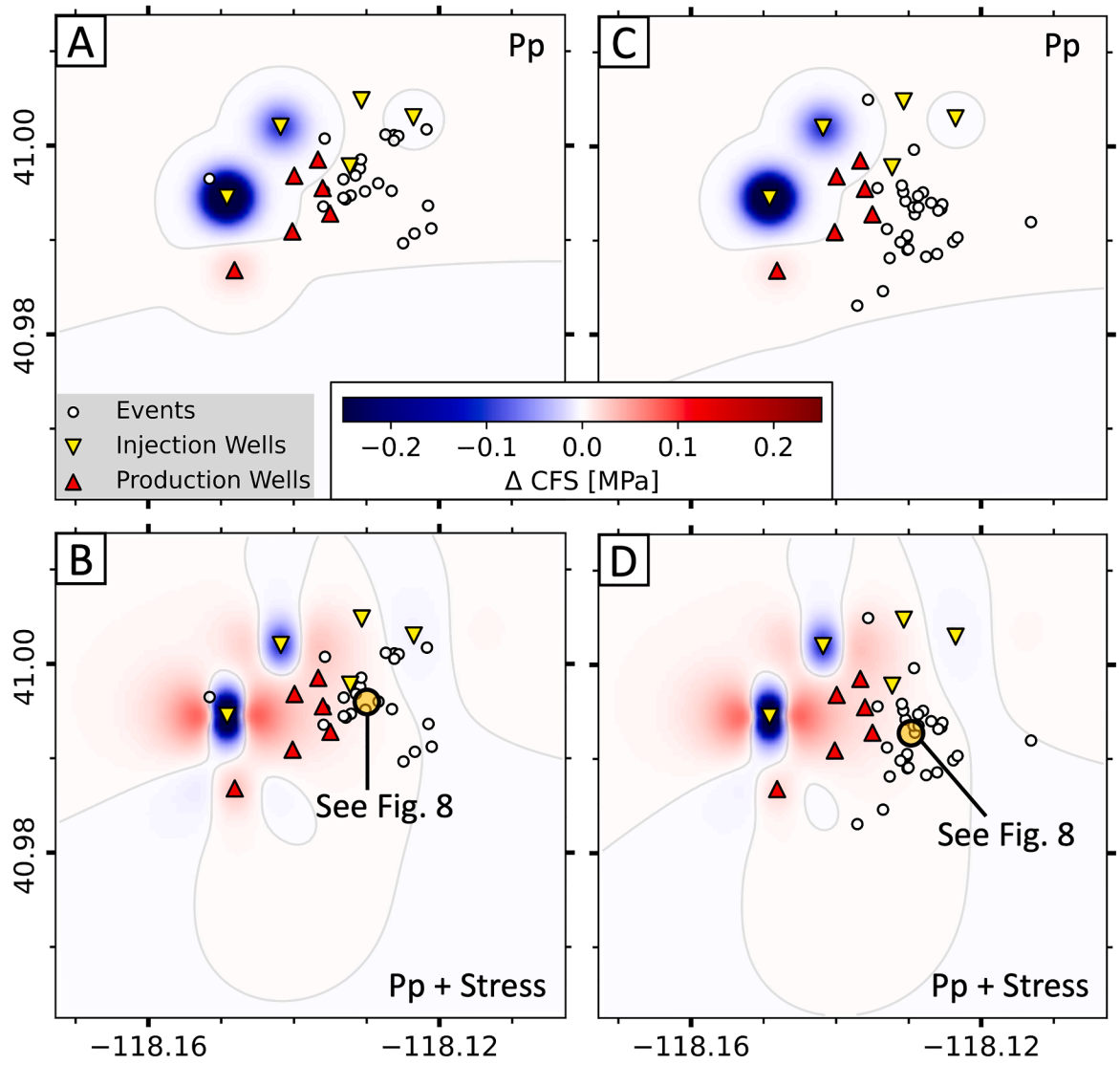

Fig. 9. Seismic response to spatial Coulomb stress changes. (A) Shows spatial distribution of Coulomb Failure Stress (CFS) changes after the 2017 shutdown at the centroid depth of the seismicity occurring during shutdown as a function of pore pressure changes. Red and blue areas indicate increase and decrease in CSR respectively. White dots represent earthquake during respective shutdowns. Solid grey lines are zero contours. (B) Similar to panel A, this shows spatial distribution of CFS changes after 2017 shutdown at the centroid depth after incorporating both pore pressure and poroelastic stress in Coulomb stress. Notably, most seismicity coincides with regions of increased CSR. Larger semitransparent orange circle represents the point in space where time series for 2017 displayed in Fig. 8 is computed. Panels (C) and (D) display the same phenomenon for 2018 shutdown similar to panels (A) and (B).

located at similar depth which further increases the effect of transient poroelastic stress changes. These observations suggest that poroelastic stressing is a primary cause for induced events during well shutdowns.

In summary, the spatiotemporal distribution of seismicity during well shutdown is well explained by fluid operation-related changes of pore pressure and poroelastic stresses and subsequent increase in Coulomb stress. The onset, amplitude, decay and distance distribution of seismicity during shutdown periods agree well with model predictions in 2018. In 2017, the model predicts two seismicity spikes similar to the observations but provides a generally poorer fit to the complex seismicity changes. The observations suggest that poroelastic coupling governs short-term induced seismicity rates during maintenance shutdowns.

Nevertheless, the contribution from short term, poroelastic transients to total seismic moment is modest. The maintenance shutdowns produced 56 events in 2017 and 45 events in 2018 with a peak magnitude of M_L 0.26 vs. a total of 277 earthquakes between 2016/10/23 and 2019/04/08. The corresponding total cumulative seismic moment over the entire time frame is 2.8×10^{11} Nm, of which only 0.1% was released during maintenance shutdowns. This difference is also reflected in the magnitudes of the largest events with M_L 1.5 for the total time frame vs. M_L 0.26 for the short term. We conclude that short-term poroelastic effects contribute only modestly to total moment release but can lead to significant short-term seismicity rate increases.

4.3. *A schematic illustration for ground subsidence and microearthquakes*

We present a schematic plot to illustrate how a geothermal reservoir reacts to both long term, steady geothermal operation and abrupt shutdowns (Fig. 10). The long-term deformation at the scale of multiple years is dominated by subsidence above the reservoir which is driven by thermal cooling and aseismic fault slip (Fig. 10a). Long-term operations are associated with low-level seismicity; however, most elastic strains are released aseismically. This long-term trend is punctuated by abrupt seismicity spikes that last several days and are caused by rapid well shutdown. The underlying driving mechanism is the effect of poroelastic

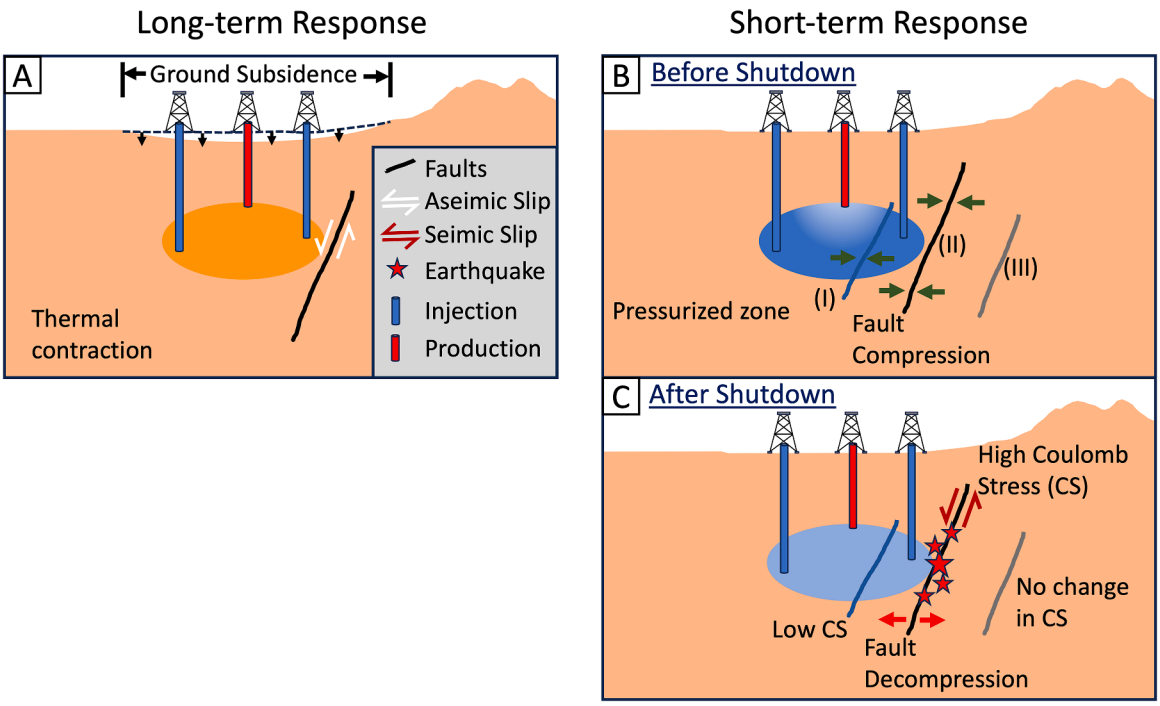

Fig. 10. Schematic representation of the response of a geothermal reservoir to long term operation and an abrupt shutdown of operational wells. A) A combination of long-term aseismic fault slip, and thermal cooling induce ground subsidence within the geothermal area. B) Faults located at closer, intermediate, and larger distance from injection wells are seismically passive during injection due to fault compression from pressure and stress. C) After the shutdown of wells, the fault at intermediate distance experiences an increase in Coulomb stress (CS) thus inducing earthquakes on the fault, whereas the fault closer to the well experiences a decline in CS and no change in CS at distant faults.

stresses which increase frictional resistance of optimally oriented normal faults during operations and fluid injection (Fig. 10b). When injection halts, faults at an intermediate distance experience a rapid drop in normal stress while pore pressures remain elevated for a prolonged period. This phenomenon leads to an increase in Coulomb stress, which ultimately drives seismic activity (Fig. 10c).

5. Conclusion

The Blue Mountain geothermal reservoir exhibits continuous long-term ground subsidence and abrupt seismicity rate spikes following well shutdowns. InSAR mapping reveals continuous surface subsidence around the geothermal reservoir, with rates reaching up to 10 mm/year. Long-term deformation is primarily aseismic and involves both localized fault slip and thermal cooling.

While long-term seismicity rates are low, sudden well shutdowns produce short term seismicity bursts. These seismic events are contained within the reservoir between 0.3 and 2.5 km depths and lack discernible alignment with preexisting faults. Pressure and stress changes due to injection and production cessation lead to higher Coulomb stresses that trigger the seismic events. The seismicity rate increase is short-lived and returns to baseline one to three days after the restart of well operations. Despite these rapid increases in seismicity rate, the geothermal reservoir generates only small magnitude events and overall low seismic hazard. Our moment balance calculation indicates that short-term poroelastic effects and associated seismicity are only a minor (4.5×10^{-6} %) component of the total observed induced deformation and comprise only 0.1% of the total seismic moment between 2016 and 2019.

The understanding of the mechanisms behind ground subsidence and microseismicity is crucial for ensuring safe geothermal operations and optimizing reservoir management. The minimal seismic activity, small event magnitudes and moderate subsidence suggest that long-term geothermal operations at Blue Mountain have limited effects on seismic and ground deformation hazards. However, short-term risks are evident. The abrupt shutdown of wells with high prior flow rates can trigger seismicity. To mitigate this risk, a gradual reduction in injection rates before well shutdown may be a viable strategy to minimize seismic activity.

CRediT authorship contribution statement

Roshan Koirala: Data curation, Formal analysis, Investigation, Methodology, Software, Validation, Visualization, Writing – original draft. **Grzegorz Kwiatek:** Software, Writing – review & editing. **Manoochehr Shirzaei:** Software, Writing – review & editing. **Emily Brodsky:** Writing – review & editing. **Trenton Cladouhos:** Writing – review & editing. **Michael Swyer:** Writing – review & editing. **Thomas Goebel:** Conceptualization, Data curation, Formal analysis, Funding acquisition, Methodology, Project administration, Resources, Software, Supervision, Validation, Visualization, Writing – review & editing.

Declaration of competing interest

The authors declare no competing interest.

Data availability

The authors do not have permission to share data.

Acknowledgement

We thank the European Space Agency (ESA) for providing SAR datasets, Cyrq Energy for sharing data on seismic monitoring and geothermal operation, and Grzegorz Kwiatek (co-author) for providing FOCI software (https://www.induced.pl/software/foci). This research was supported by the Department of Energy grant DE-SC0015539 to Thomas Goebel. Manoochehr Shirzaei's contribution is supported by the

Department of Energy Grant DE-SC0019307.

Supplementary materials

Supplementary material associated with this article can be found, in the online version, at doi:10.1016/j.epsl.2024.118883.

References

Bakun, W.H., Joyner, W.B., 1984. The ML scale in central California. Bull. Seismol. Soc. Am. 74 (5), 1827–1843. https://doi.org/10.1785/BSSA0740051827.

Casteel, J., Trazona, R., Melosh, G., Niggemann, K., Fairbank, B., 2009. A preliminary conceptual model for the Blue Mountain geothermal system, Humboldt County, Nevada. Trans. - Geotherm. Resour. Counc. 33 (April), 809–812.

Chang, K.W., Segall, P., 2016. Injection-induced seismicity on basement faults including poroelastic stressing. J. Geophys. Res. Solid Earth 121 (4), 2708–2726. https://doi.org/10.1002/2015JB012561.

Clauset, A., Shalizi, C.R., Newman, M.E.J., 2009. Power-Law distributions in empirical data. SIAM Rev. 51 (4), 661–703. https://doi.org/10.1137/070710111.

Costantini, M., 1998. A novel phase unwrapping method based on network programming. IEEE Trans. Geosci. Remote Sens. 36 (3), 813–821. https://doi.org/10.1109/36.673674.

Costantini, M., Rosen, P.A., 1999. A generalized phase unwrapping approach for sparse data. IEEE 1999 International Geoscience and Remote Sensing Symposium. IGARSS'99 (Cat. No.99CH36293) 1, 267–269. https://doi.org/10.1109/IGARSS.1999.773467.

De Barros, L., Guglielmi, Y., Cappa, F., Nussbaum, C., Birkholzer, J., 2023. Induced microseismicity and tremor signatures illuminate different slip behaviors in a natural shale fault reactivated by a fluid pressure stimulation (Mont Terri). Geophys. J. Int. ggad231. https://doi.org/10.1093/gji/ggad231.

Deichmann, N., Giardini, D., 2009. Earthquakes induced by the stimulation of an enhanced geothermal system below Basel (Switzerland). Seismol. Res. Lett. 80 (5), 784–798. https://doi.org/10.1785/gssrl.80.5.784.

Dieterich, J., 1994. A constitutive law for rate of earthquake production and its application to earthquake clustering. J. Geophys. Res. Solid Earth 99 (B2), 2601–2618. https://doi.org/10.1029/93JB02581.

Faulds, J.E., Hinz, N.H., Dering, G.M., Siler, D.L., 2013. The hybrid model - The most accommodating structural setting for geothermal power generation in the Great Basin, western USA. Trans. - Geotherm. Resour. Counc. 37 (PART 1), 3–10.

Faulds, J.E., Melosh, G., 2008. A preliminary structural model for the blue mountain geothermal field, Humboldt County, Nevada. Trans. Geothermal Resour. Council, pp. 234–239.

Fialko, Y., Simons, M., 2000. Deformation and seismicity in the Coso geothermal area, Inyo County, California: observations and modeling using satellite radar interferometry. J. Geophys. Res. Solid Earth 105 (B9), 21781–21793. https://doi.org/10.1029/2000JB900169.

Gaucher, E., Schoenball, M., Heidbach, O., Zang, A., Fokker, P.A., van Wees, J.-D., Kohl, T., 2015. Induced seismicity in geothermal reservoirs: a review of forecasting approaches. Renew. Sustain. Energy Rev. 52, 1473–1490. https://doi.org/10.1016/j.rser.2015.08.026.

Goebel, T.H.W., Brodsky, E.E., 2018. The spatial footprint of injection wells in a global compilation of induced earthquake sequences. Science 361 (6405), 899–904. https://doi.org/10.1126/science.aat5449.

Goebel, T.H.W., Weingarten, M., Chen, X., Haffener, J., Brodsky, E.E., 2017. The 2016 Mw5.1 Fairview, Oklahoma earthquakes: evidence for long-range poroelastic triggering at >40 km from fluid disposal wells. Earth Planet. Sci. Lett. 472, 50–61. https://doi.org/10.1016/j.epsl.2017.05.011.

Grigoli, F., Cesca, S., Rinaldi, A.P., Manconi, A., López-Comino, J.A., Clinton, J.F., Westaway, R., Cauzzi, C., Dahm, T., Wiemer, S., 2018. The November 2017 M_w 5.5 Pohang earthquake: a possible case of induced seismicity in South Korea. Science 360 (6392), 1003–1006. https://doi.org/10.1126/science.aat2010.

Guo, H., Brodsky, E.E., Goebel, T.H.W., Cladouhos, T.T., 2021. Measuring fault zone and host rock hydraulic properties using tidal responses. Geophys. Res. Lett. 48 (13), e2021GL093986 https://doi.org/10.1029/2021GL093986.

Hanssen, R.F., 2001. Radar Interferometry: Data Interpretation and Error Analysis. Springer Netherlands, Dordrecht, Remote Sensing and Digital Image Processing. https://doi.org/10.1007/0-306-47633-9.

Hsieh, P.A., Bredehoeft, J.D., 1981. A reservoir analysis of the Denver earthquakes: A case of induced seismicity. J. Geophys. Res. Solid Earth 86, no. B2 903–920. https://doi.org/10.1029/JB086iB02p00903.

International Energy Agency, 2011. Technology Roadmap: Geothermal Heat and Power. OECD Publishing, IEA Technology Roadmaps. https://doi.org/10.1787/9789264118485-en.

Juncu, D., Árnadóttir, Th., Hooper, A., Gunnarsson, G., 2017. Anthropogenic and natural ground deformation in the Hengill geothermal area, Iceland. J. Geophys. Res. Solid Earth 122 (1), 692–709. https://doi.org/10.1002/2016JB013626.

Kamali-Asl, A., Ghazanfari, E., Perdrial, N., Cladouhos, T., 2020. Effects of injection fluid type on pressure-dependent permeability evolution of fractured rocks in geothermal reservoirs: an experimental chemo-mechanical study. Geothermics 87, 101832. https://doi.org/10.1016/j.geothermics.2020.101832.

Keranen, K.M., Weingarten, M., 2018. Induced seismicity. Annu. Rev. Earth Planet. Sci. 46 (1), 149–174. https://doi.org/10.1146/annurev-earth-082517-010054.

Kim, K.-H., Ree, J.-H., Kim, Y., Kim, S., Kang, S.Y., Seo, W., 2018. Assessing whether the 2017 Mw 5.4 Pohang earthquake in South Korea was an induced event. Science 360 (6392), 1007–1009. https://doi.org/10.1126/science.aat6081.

Kwiatek, G., (2020). FOCI [computer software, retreved from https://www.induced.pl/software/foci].

Lee, J.-C., Shirzaei, M., 2023. Novel algorithms for pair and pixel selection and atmospheric error correction in multitemporal InSAR. Remote Sens. Environ. 286, 113447 https://doi.org/10.1016/j.rse.2022.113447.

Lomax, A., Michelini, A., Curtis, A., 2009. Earthquake location, direct, global-search methods. In: Meyers, R.A. (Ed.), Encyclopedia of Complexity and Systems Science. Springer, New York, NY, pp. 1–33. https://doi.org/10.1007/978-3-642-27737-5_150-2. Editor.

Lomax, A., J. Virieux, P. Volant, and C. Berge-Thierry (2000). Probabilistic earthquake location in 3D and layered models, in Advances in Seismic Event Location C.H. Thurber, and N. Rabinowitz (Editors), Springer Netherlands, Dordrecht, Modern Approaches in Geophysics, 101–134, doi: 10.1007/978-94-015-9536-0_5.

Lund, J.W., Toth, A.N., 2021. Direct utilization of geothermal energy 2020 worldwide review. Geothermics 90, 101915. https://doi.org/10.1016/j.geothermics.2020.101915.

Majer, E.L., Baria, R., Stark, M., Oates, S., Bommer, J., Smith, B., Asanuma, H., 2007. Induced seismicity associated with enhanced geothermal systems. Geothermics 36 (3), 185–222. https://doi.org/10.1016/j.geothermics.2007.03.003.

Martínez-Garzón, P., Kwiatek, G., Sone, H., Bohnhoff, M., Dresen, G., Hartline, C., 2014. Spatiotemporal changes, faulting regimes, and source parameters of induced seismicity: a case study from The Geysers geothermal field. J. Geophys. Res. Solid Earth 119 (11), 8378–8396. https://doi.org/10.1002/2014JB011385.

Materna, K., Barbour, A., Jiang, J., Eneva, M., 2022. Detection of aseismic slip and poroelastic reservoir deformation at the North Brawley geothermal field from 2009 to 2019. J. Geophys. Res. Solid Earth 127 (5), e2021JB023335. https://doi.org/10.1029/2021JB023335.

Matzel, Dennise Templeton, Chiorini, Sutton, Cladouhos, Trenton, 2019. Imaging the blue mountain geothermal site using seismic interferometry. In: Proceedings of the 44th Workshop on Geothermal Reservoir Engineering Stanford University. Stanford, California.

Mcgarr, A., 1976. Seismic moments and volume changes. J. Geophys. Res. 81, 1487–1494. https://doi.org/10.1029/JB081i008p01487.

Miller, M.M., Shirzaei, M., 2015. Spatiotemporal characterization of land subsidence and uplift in Phoenix using InSAR time series and wavelet transforms. J. Geophys. Res. Solid Earth 120 (8), 5822–5842. https://doi.org/10.1002/2015JB012017.

Mogi, K. (1958). Relations between the Eruptions of Various Volcanoes and the Deformations of the Ground Surfaces around them.

Mossop, A., Segall, P., 1997. Subsidence at The Geysers Geothermal Field, N. California from a comparison of GPS and leveling surveys. Geophys. Res. Lett. 24 (14), 1839–1842. https://doi.org/10.1029/97GL51792.

Okada, Y., 1985. Surface deformation due to shear and tensile faults in a half-space. Bull. Seismol. Soc. Am. 75 (4), 1135–1154. https://doi.org/10.1785/BSSA0750041135.

Pierre, J.Rutqvist, Dobson, P.F., Walters, M., Hartline, C., Garcia, J., 2014. The impacts of mechanical stress transfers caused by hydromechanical and thermal processes on fault stability during hydraulic stimulation in a deep geothermal reservoir. Int. J. Rock Mech. Min. Sci. 72, 149–163. https://doi.org/10.1016/j.ijrmms.2014.09.005.

Pijnenburg, R.P.J., Verberne, B.A., Hangx, S.J.T., Spiers, C.J., 2018. Deformation behavior of sandstones from the seismogenic groningen gas field: role of inelastic versus elastic mechanisms. J. Geophys. Res. Solid Earth 123 (7), 5532–5558. https://doi.org/10.1029/2018JB015673.

Prieto, G.A., 2022. The multitaper spectrum analysis package in python. Seismol. Res. Lett. 93 (3), 1922–1929. https://doi.org/10.1785/0220210332.

Rudnicki, J.W., 1986. Fluid mass sources and point forces in linear elastic diffusive solids. Mech. Mater. 5 (4), 383–393. https://doi.org/10.1016/0167-6636(86)90042-6.

Segall, P., 2010. Earthquake and Volcano Deformation. Princeton University Press.

Segall, P., 1989. Earthquakes triggered by fluid extraction. Geology 17 (10), 942–946. https://doi.org/10.1130/0091-7613(1989)017<0942:ETBFE>2.3.CO;2.

Segall, P., Grasso, J.-R., Mossop, A., 1994. Poroelastic stressing and induced seismicity near the LACQ gas field, southwestern France. J. Geophys. Res. Solid Earth 99 (B8), 15423–15438. https://doi.org/10.1029/94JB00989.

Segall, P., Lu, S., 2015. Injection-induced seismicity: poroelastic and earthquake nucleation effects. J. Geophys. Res. Solid Earth 120 (7), 5082–5103. https://doi.org/10.1002/2015JB012060.

Shirzaei, M., 2013. A wavelet-based multitemporal DInSAR algorithm for monitoring ground surface motion. IEEE Geosci. Remote Sens. Lett. 10 (3), 456–460.

Shirzaei, M., Bürgmann, R., 2012. Topography correlated atmospheric delay correction in radar interferometry using wavelet transforms. Geophys. Res. Lett. 39 (1) https://doi.org/10.1029/2011GL049971.

Shirzaei, M., Bürgmann, R., Fielding, E.J., 2017. Applicability of Sentinel-1 Terrain Observation by Progressive Scans multitemporal interferometry for monitoring slow ground motions in the San Francisco Bay Area. Geophys. Res. Lett. 44 (6), 2733–2742. https://doi.org/10.1002/2017GL072663.

Shirzaei, M., Walter, T.R., 2011. Estimating the effect of satellite orbital error using wavelet-based robust regression applied to InSAR deformation data. IEEE Trans. Geosci. Remote Sens. 49 (11), 4600–4605. https://doi.org/10.1109/TGRS.2011.2143419.

Swyer, M., 2021. Stimulation of a sub-commercial geothermal well by long-term, low-flow injection at blue mountain geothermal field, Nevada. GRC Trans 45.

Trugman, D.T., Shearer, P.M., 2017. GrowClust: a hierarchical clustering algorithm for relative earthquake relocation, with application to the spanish springs and Sheldon,

Nevada, earthquake sequences. Seismol. Res. Lett. 88 (2A), 379–391. https://doi.org/10.1785/0220160188.

Wang, T.A., Dunham, E.M., 2022. Hindcasting injection-induced aseismic slip and microseismicity at the cooper basin enhanced geothermal systems project. Sci. Rep. 12 (1), 19481. https://doi.org/10.1038/s41598-022-23812-7.

Wei, S., Avouac, J.-P., Hudnut, K.W., Donnellan, A., Parker, J.W., Graves, R.W., Helmberger, D., Fielding, E., Liu, Z., Cappa, F., et al., 2015. The 2012 Brawley swarm triggered by injection-induced aseismic slip. Earth Planet. Sci. Lett. 422, 115–125. https://doi.org/10.1016/j.epsl.2015.03.054.

Wiemer, S., 2000. Minimum magnitude of completeness in earthquake catalogs: examples from Alaska, the Western United States, and Japan. Bull. Seismol. Soc. Am. 90 (4), 859–869. https://doi.org/10.1785/0119990114.

Wyld, S.J., 2002. Structural evolution of a Mesozoic backarc fold-and-thrust belt in the U. S. Cordillera: new evidence from northern Nevada. Bull. Geol. Soc. Am. 114 (11), 1452–1468. https://doi.org/10.1130/0016-7606(2002)114<1452:SEOAMB>2.0.CO;2.

Zhai, G., Shirzaei, M., Manga, M., 2021. Widespread deep seismicity in the Delaware Basin, Texas, is mainly driven by shallow wastewater injection. Proc. Natl. Acad. Sci 118 (20), e2102338118. https://doi.org/10.1073/pnas.2102338118.

Zhang, Y., Xiang, W., Liu, G., Wang, X., Zhang, R., Zhang, X., Tong, J., Yuan, H., Zhang, C., 2023. Geodetic imaging of ground deformation and reservoir parameters at the Yangbajing Geothermal Field, Tibet, China. Geophys. J. Int. 234 (1), 379–394. https://doi.org/10.1093/gji/ggad018.